



**Barriers and chutes for mixing of active particles in a vortex chain flow**Nghia Le,<sup>1</sup> Casey M. Miller,<sup>1</sup> Julianna S. Detrick,<sup>1</sup> Cameron R. Lodi,<sup>1</sup>  
Kevin A. Mitchell ,<sup>2</sup> and Thomas H. Solomon <sup>1,\*</sup><sup>1</sup>*Department of Physics & Astronomy, Bucknell University, Lewisburg, Pennsylvania 17837, USA*<sup>2</sup>*Department of Physics, University of California, Merced, California 95343, USA*

(Received 10 June 2022; accepted 25 March 2024; published 3 May 2024)

We present experiments on the mixing of active particles—swimming *Tetraselmis* microbes—in a microfluidic vortex chain flow, driven magnetohydrodynamically. We track the microbes in the flow and interpret the resulting trajectories in terms of a theory of swimming invariant manifolds (SwIMs), a generalization of invariant manifold theories developed originally to characterize mixing of passive tracers. The experiments verify predictions that SwIMs act as barriers in a three-dimensional  $(x, y, \theta)$  phase space. Projected onto  $(x, y)$  position space, edges of the manifolds (SwIM-edges) are one-way barriers that impede the motion of the microbes in one direction but allow them to pass freely in the other. Pairs of SwIMs combine to form chutes that carry microbes between vortices. For short times, the experimentally measured intervortex flux agrees well with theoretical predictions based on the cross-sectional area of the chutes, despite experimental evidence of nonuniformities in the  $(x, y, \theta)$  microbe density, due to deviations of the microbes from a perfect circular shape.

DOI: [10.1103/PhysRevFluids.9.054501](https://doi.org/10.1103/PhysRevFluids.9.054501)**I. INTRODUCTION**

There has been significant interest recently in *active* matter systems [1], defined as those with an internal energy source, including self-propelled particles such as swimming microbes [2] and artificial swimmers [3–5]. This is a problem with potential applications to a wide range of systems such as self-assembly of active colloids [6] and the use of active particles for drug delivery [7]. In nature and in many technical and industrial processes, there are imposed fluid flows that impact the behavior of these active agents such as in harmful algal blooms in the oceans [8] and the motion of charged particles in plasma flows [9]. Mixing of active agents in a flow has recently received attention in studies of the varying densities of swimming microbes in channel flows [10–13], the behavior of active agents in porous flows [11], and the effects of swimming microbes on the transport and mixing of passive impurities [14–18].

Previous studies by our group have identified “burning invariant manifolds” (BIMs) that act as one-way barriers that inhibit the motion of propagating chemical reactions in a wide range of two- and three-dimensional laminar flows [19–25]. A similar theory predicts “swimming invariant manifolds” (SwIMs) that block the motion of swimming particles in the same flows [12,26,27]. Experimentally, we have demonstrated that microbes swimming in an open, two-dimensional, hyperbolic flow are blocked by SwIMs in a three-dimensional phase space determined by the  $x$  and  $y$  coordinates and the swimming direction  $\theta$  of the microbes. Projected into  $(x, y)$  position space, edges of these SwIMs act as one-way barriers to microbe motion, similar to how BIMs act as one-way barriers blocking the motion of reaction fronts. An open question is how SwIMs

---

\*Corresponding author: [tsolomon@bucknell.edu](mailto:tsolomon@bucknell.edu)

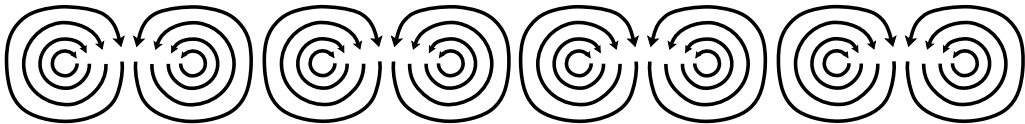


FIG. 1. Chain of alternating vortices.

affect transport and mixing for active particles in closed, cellular flows with no long-range passive transport.

In this article, we explore the mixing of swimming microbes in a laminar, two-dimensional, time-independent vortex chain flow. The microbes are *Tetraselmis*, eukaryotic algae that swim with the use of four pulling flagella. We analyze the mixing of the microbes with the swimming invariant manifold theoretical framework, testing in particular the blocking behavior of SwIMs and SwIM edges. Furthermore, tubes (*chutes*) formed by combinations of the SwIMs provide a mechanism for exchange of the microbes between vortices, leading to long-range transport. We explore reorientation of the swimming direction by the flow due to the nonspherical shape of the microbes and possibly any influence of the flagella. In addition, we find variations in densities for active particle trajectories in  $(x, y, \theta)$  phase space.

The flow studied in this paper is a very simple, well-ordered flow. And the SwIM theory makes simplifying assumptions about the motions of the microbes as well. And yet there are real systems that are comparable to these studies, including cellular-scale and other microfluidic flows with small Reynolds number. Even for higher Reynolds number flows such as flows in the oceans and atmosphere, vortex flows are very common in nature, even if not perfectly spatially periodic or time-independent. Furthermore, this work is foundational; in general, laminar flows are composed of a combination of jet/channel, hyperbolic, and elliptical flows. Previous experiments have explored the mixing of active particles in channel [10,13] and hyperbolic [26,27] flows. But studies of mixing of active particles in vortex flows are lacking. Furthermore, the experiments in this paper deviate from the simplified conditions of the theory, giving us the opportunity to explore the robustness of the theory to describe real systems. Ultimately, a better understanding of the simplified cases will lead to insights into the behavior of a wide range of active particles in realistic fluid flows, similar to how studies [28–34] of manifolds and lobes for passive mixing in 1980s and 1990s have led more recently to theories (and experiments) about Lagrangian Coherent Structures [35–37] for passive mixing in aperiodic and turbulent flows.

In Sec. II, we discuss the theory and present simulations of swimming invariant manifolds. We also discuss the chute mechanism responsible for cross-vortex mixing. The experimental techniques and methods are presented in Sec. III. The experimental results are presented in Sec. IV. We discuss the results and comment about continuing studies in Sec. V.

## II. THEORY

The flow studied in these experiments is composed of a chain of alternating vortices, as sketched in Fig. 1. For the simulations we assume a simplified model of the velocity field that assumes free-slip boundary conditions:

$$\begin{aligned} u_x &= U \sin(\pi x/L) \cos(\pi y/L), \\ u_y &= -U \cos(\pi x/L) \sin(\pi y/L). \end{aligned} \quad (1)$$

In these expressions,  $U$  is the maximum flow speed (in the middle of the vortex separatrices) and  $L$  is the length and height of the vortices. Unless otherwise stated, the  $x$  and  $y$  coordinates in this article are normalized by  $L$  such that the nondimensional  $y$  goes from 0 to 1 across one vortex and the nondimensional  $x$  goes from 0 to 2 across a pair of vortices. In the experiments, the flow has no-slip boundary conditions at  $y = 0$  and 1, resulting in a velocity field that drops to zero at these

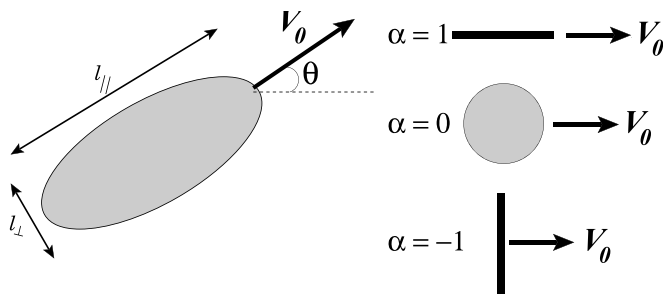


FIG. 2. Spheroidal model of a swimming microbe with length and width  $l_{\parallel}$  and  $l_{\perp}$ , respectively. The angle  $\theta$  denotes the direction at which the microbe swims (at speed  $V_0$ ), and the parameter  $\alpha$  denotes the shape.

boundaries. The theoretical flow of Eqs. (1) also does not include a weak, 3D flow due to Ekman pumping [34] in the experiments that circulates fluid in toward the vortex centers at the top and bottom surfaces and back outward at the midheight.

Passive mixing has been studied extensively in vortex chain and vortex array flows. Numerically, passive trajectories are determined by integrating the velocity field  $\dot{x} = u_x$  and  $\dot{y} = u_y$ . For a two-dimensional, time-independent flow, passive trajectories are all ordered and invariant manifolds of the hyperbolic fixed points (at the corners of the vortices) coincide with the vortex separatrices, forming barriers that prevent transport in either direction between vortices in the absence of molecular diffusion. If the flow is time-dependent, the phase space for particle trajectories is three-dimensional  $(x, y, t)$  and chaotic advection is possible [38,39]; passive invariant manifolds [28] and invariant tori continue to act as barriers that block mixing, and lobes formed by intersections of invariant manifolds provide a mechanism for transport between unit cells of the flow [32,33,40].

For a self-propelled tracer, we consider a simplified spheroidal particle (Fig. 2) with aspect ratio  $\gamma = l_{\parallel}/l_{\perp}$  and  $\alpha = \frac{\gamma^2-1}{\gamma^2+1}$  that swims with a constant speed  $V_0$ ; we define a nondimensional swimming speed  $v_0 = V_0/U$  for the vortex flow. The microbes in these experiments (see Sec. III) are not idealized spheroids, and there are also questions about the effects of the flagella on  $\alpha$ . Furthermore, the swimming speeds are not constant as is assumed in the theory.

For a swimmer, the phase space is three-dimensional, parametrized by the  $x$  and  $y$  coordinates and the swimming direction  $\theta$ . The motion of the swimmer in an external flow is governed by the equations [26,41–44]

$$\begin{aligned} \dot{x} &= u_x + V_0 \cos \theta, & \dot{y} &= u_y + V_0 \sin \theta, \\ \dot{\theta} &= (\omega/2) + \alpha \left[ \frac{1}{2}(u_{x,y} + u_{y,x}) \cos 2\theta - u_{x,x} \sin 2\theta \right], \end{aligned} \quad (2)$$

where the vorticity  $\omega = u_{y,x} - u_{x,y}$ . The theory assumes smooth-swimming microbes that move with constant speed and with no spontaneous active tumbling (i.e., tumbling due to the organism itself, not due to the flow) nor any translational or rotational noise. Any changes in swimming direction are due only to interactions with the flow.

We define a swimming fixed point (SFP) as a location in  $(x, y, \theta)$  space where  $\dot{x}$ ,  $\dot{y}$  and  $\dot{\theta}$  are all zero. These are distinct from the advective fixed points where the fluid velocity  $\mathbf{u}$  vanishes. Typically, if the swimming speed is not too large, there will be four swimming fixed points surrounding a hyperbolic advective fixed point, two for particles swimming toward the advective fixed point and two for particles swimming away from the advective fixed point. The black dots in Fig. 3(a) are two such swimming fixed points in the full phase space. They project to the two black dots in position space in Fig. 3(b). The bottom swimming fixed point corresponds to a swimmer swimming to the right, away from the advective fixed point [open circle in Fig. 3(b)]. The top swimming fixed point also corresponds to a swimmer swimming to the right, which in this case is toward the advective fixed point. The bottom swimming fixed point has stability stable-unstable-unstable (SUU). The

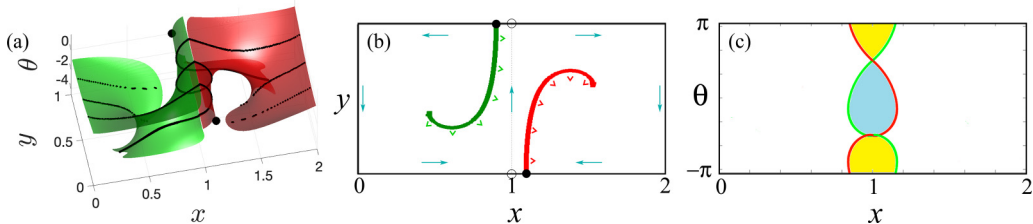


FIG. 3. (a) Simulated stable (unstable) manifold in  $(x, y, \theta)$ -space for self-propelled particles, shown in green (red), along with swimming fixed points (black dots);  $\alpha = 0.3$  and  $v_0 = 0.3$ . Cross-sections of the manifolds in thin slices around  $y = 0.25, 0.50$ , and  $0.75$  are plotted in black. (b) SwIM edges in  $(x, y)$ -space for the manifolds in panel (a). The carets show the blocking direction of the SwIM edges, the dotted line shows the separatrix between adjacent vortices, the open circles show the advective fixed points, and the green arrows show the flow direction. (c)  $(x, \theta)$  cross-sections at  $y = 0.5$  of stable and unstable SwIMs (curves colored green and red, respectively) that form the chutes between two vortices, including those for the left-going chute not shown in (a). Cross-sections of the right-going and left-going chutes are shaded in as light blue and yellow, respectively.

2D red sheet in Fig. 3(a) is a finite piece of the unstable manifold of the bottom fixed point. The top swimming fixed point has opposite stability, stable-stable-unstable (SSU). The 2D green sheet in Fig. 3(a) is a finite piece of its stable manifold. We call these 2D sheets *swimming invariant manifolds* (SwIMs). Since these sheets are codimension one, they are absolute barriers to transport in the full 3D phase space. Projections of the folds of the SwIMs into  $(x, y)$  space are also shown in Fig. 3(b). We call these “SwIM edges.”

To compute the red unstable manifold, we first find two heteroclinic orbits from the SUU SFP shown in Fig. 3(a) to the two nearby SSU SFPs. These orbits form a 1D curve within the unstable manifold. Then trajectories are launched from the vicinity of this 1D curve. These trajectories naturally sweep out the full unstable manifold. The green stable manifold is obtained via a symmetric rotation applied to the unstable manifold.

Projected into  $(x, y)$  space [Fig. 3(b)], the bottom SFP (with swimming direction  $\theta = 0$ ) corresponds to a microbe swimming to the right but motionless since the fluid velocity at that point is equal and opposite to the swimming velocity. If the microbe is swimming to the left, however, it passes through the  $(x, y)$  projection of the bottom SFP. Remarkably, this property holds to a surprising degree along the length of the SwIM edges [26]. That is, the SwIM edges act as one-way barriers blocking microbes swimming in the directions denoted by the carets in Fig. 3(b), but allowing microbes to swim across in the opposite direction. These rules apply whether the swimmer approaches the SwIM edge at a right angle or more obliquely. In a strict mathematical sense, the one-way barrier nature of a SwIM holds in the neighborhood of the fixed point, but in practice it holds essentially along the entire length of the SwIM edge plotted.

The one-way blocking nature of the SwIM edges is shown numerically in Fig. 4, which shows a 3D SwIM in  $(x, y, \theta)$  space, along with a swimmer trajectory that starts at the black dot to the left of the SwIM. The swimmer moving to the right with a swimming orientation near  $\theta = 0$  ends up caught in the curved portion of the SwIM and cannot pass through. But as the swimmer trajectory moves around the SwIM, the curved portion opens up and flattens. The trajectory curves around with the swimmer ultimately swimming with orientation  $\theta$  near  $\theta = -\pi$ , enabling it to pass underneath the curved portion of the SwIM and move back to the left. When projected into  $(x, y)$  [Fig. 4(b)], the microbe goes around the SwIM edge when moving toward the right, but it passes *through* the SwIM edge when going to the left. This is the basic mechanism by which SwIM edges act as one-way barriers in  $(x, y)$  space.

The stable and unstable SwIMs collectively form tube-like chutes [Fig. 3(a)] that account for cross-vortex transport of active particles for the time-independent vortex chain. Any self-propelled

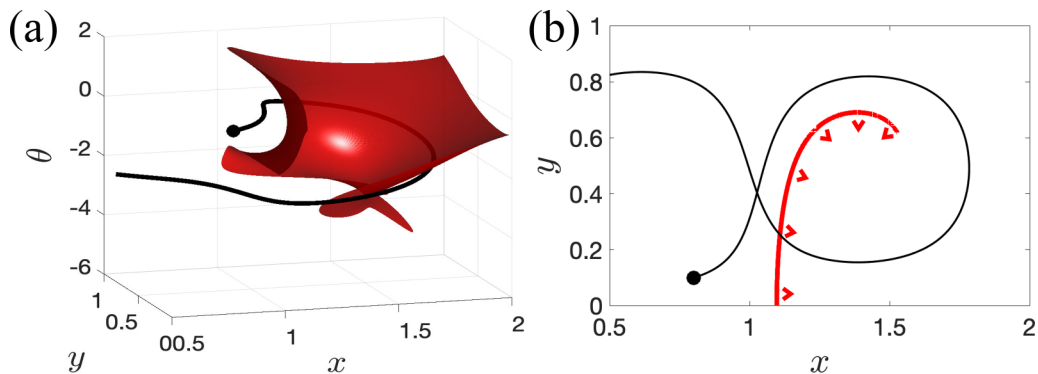


FIG. 4. (a) Numerically calculated swimming invariant manifold (SwIM) in  $(x, y, \theta)$ , with a sample trajectory. A rotating movie of this image (Movie1.avi) can be found online in Supplemental Material [46]. (b) SwIM edge for the SwIM from figure (a), along with projection of the trajectory in  $(x, y)$ . For panels (a) and (b), the black dot represents the beginning of the trajectory.

particle that enters the chute in  $(x, y, \theta)$  crosses from one vortex to the next. There are two chutes that enable transport across each separatrix. Figure 3(a) shows the chute responsible for transport to the right, whereas there is another chute (not shown) around  $\theta = \pm\pi$  that corresponds to transport to the left. An  $(x, \theta)$  cross-section of both of these chutes at  $y = 0.5$  is shown in Fig. 3(c). The cross section of the right-going chute is shaded light blue, with the left-going cross section [which is split between  $\theta = \pi$  and  $-\pi$  in Fig. 3(c)] shaded yellow.

A prediction of cross-vortex active transport is made by considering particles passing through these chute cross sections. Over a small time  $t$ , tracers in the  $(x, \theta)$  cross-section move in the  $y$ -direction with a phase space speed  $\dot{y}(x, \theta)$  locally. The volume swept out by the chute cross-section during a small time  $t$  is  $V(t) = \int_{\text{chute}} \dot{y}(x, \theta) t dA$  where the integral is over the area of the chute cross-section. Dividing this swept volume by the total volume  $2\pi L^2$  for a single vortex in  $(x, y, \theta)$  and taking a time derivative, we arrive at the flux  $F$  (fraction  $f$  of tracers in a vortex leaving per unit time):

$$F = df/dt = \frac{1}{2\pi L^2} \int_{\text{chute}} \dot{y} dA. \quad (3)$$

This prediction is valid only for small times and assumes uniform particle densities in  $(x, y, \theta)$  space, valid theoretically for perfectly circular ( $\alpha = 0$ ) particles with no flagella.

The structures shown in Figs. 3 and 4 do not show all of the important blocking and guiding structures in the flow. There are many more swimming fixed points (SFPs) than the two shown in Fig. 3 as black dots. Each vortex corner has three SFPs. (If this were a vortex array, then each corner would have four SFPs.) For instance, in addition to the SFP shown in Fig. 3(a) to the right of the vortex corner at  $(x, y, \theta) = (1.1, 0.0, 0.0)$ , there is another SFP that is not shown at  $(x, y, \theta) = (0.9, 0.0, \pi)$ . Similarly, the SwIM shown in red attached to the fixed point in Fig. 3(a) has a corresponding SwIM which is not shown attached to the (not shown) SFP at  $(0.9, 0.0, \pi)$ . Both of these SwIMs (the red one and the one not shown in Fig. 3) block active particles swimming away from the separatrix between the vortices. Furthermore, there is another SFP and SwIM (also not shown) near  $(x, y, \theta) = (1.0, 0.1, -\pi/2)$  that block swimmers swimming downward toward the bottom vortex corner. Similarly, there are three SFPs and SwIMs around every vortex corner in the flow. There are also invariant tori near the advective fixed points at the vortex centers [45]. The combination of all of these SwIMs forms a complex network of barriers that block swimming motion and form chutes throughout the flow. Furthermore, there are also mixing barriers due to

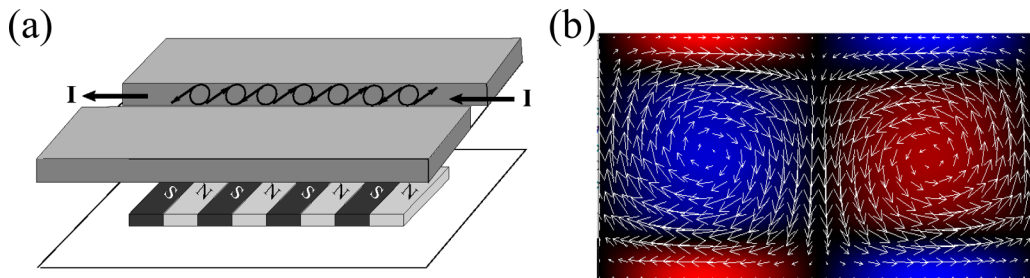


FIG. 5. (a) Exploded view of experimental apparatus, showing the magnetohydrodynamic forcing technique. (b) Experimentally determined velocity field (white arrows) and vorticity field (red and blue shading).

invariant tori [47] separating regions of ordered and chaotic motion of microbes in the flow. We focus primarily on the SwIMs near the vortex boundaries in these experiments.

### III. EXPERIMENTAL METHODS

#### A. Flow apparatus

Experimentally, the vortex flow is driven using a magnetohydrodynamic technique [33,48] [Fig. 5(a)]. A channel ( $1.0 \text{ mm} \times 1.0 \text{ mm}$  cross section) milled into acrylic holds salt water with the swimming microbes. A chain of  $1.0 \text{ mm}$  wide Nd-Fe-B magnets (grade N35 with maximum field strength  $1.2 \text{ T}$ ) with alternating polarity is below the channel. A glass cover slip covers the channel, the entire cell is inverted and the flow region is imaged from below with a Nikon Eclipse inverted microscope. A  $1.0\text{--}2.0 \text{ mA}$  DC electrical current passes through the fluid and interacts with the alternating magnetic field to produce a chain of vortices with maximum flow speed  $U$  ranging from  $300\text{--}800 \mu\text{m/s}$ . In addition to the current and the magnetic field strength, the flow speeds also depend on the distance between the magnets and the fluid region, which can vary slightly between different cells based on slight variations in the milling.

The system is observed with two different microscope objectives. With a  $4\times$  objective, the field of view is roughly  $3 \text{ mm}$ , with three vortices visible in the chain. With a  $2\times$  objective, the field of view is roughly  $6 \text{ mm}$  with six vortices visible. The velocity field for this flow [Fig. 5(b), measured at  $4\times$  magnification] is measured using particle tracking velocimetry. Unlike for the free-slip model [Eq. (1)], there are no-slip boundary conditions at the top and bottom due to the rigid sidewalls of the channel. The no-slip boundary conditions create regions of vorticity at the top and bottom that are opposite the vorticity in the vortex centers.

#### B. Microbes

The self-propelled particles in the experiment are *Tetraselmis* [Fig. 6(a)], green marine algae that are almost circular with a typical diameter of  $10\text{--}15 \mu\text{m}$ . The *Tetraselmis* are purchased from Carolina Biological Supply (Catalog No. 152610), which was originally sourced from Florida Aqua Farms; years of culturing have made the line distinct. In our laboratory,  $1 \text{ ml}$  of the culture from Carolina is combined with  $150 \text{ ml}$  of “Alga-Gro Seawater” medium, cultured for 2 weeks under a dedicated fluorescent lamp and then transferred to  $15 \text{ ml}$  centrifuge tubes from which samples are drawn.

We estimate  $\alpha$  to be approximately  $0.3$  for the *Tetraselmis*, neglecting the flagella. We have no direct measurements—or even visualization—of the flagella, but *Tetraselmis* is well-known to have four pulling flagella that perform a breast-stroke motion to propel the microbe. The swimming speed in the absence of an imposed flow varies from one microbe to the next [Fig. 6(b)] with typical average speeds between  $150$  and  $250 \mu\text{m/s}$ . The swimming speed for an individual microbe also varies during its motion, as shown in Fig. 6(c), with standard deviations ranging up to about half of



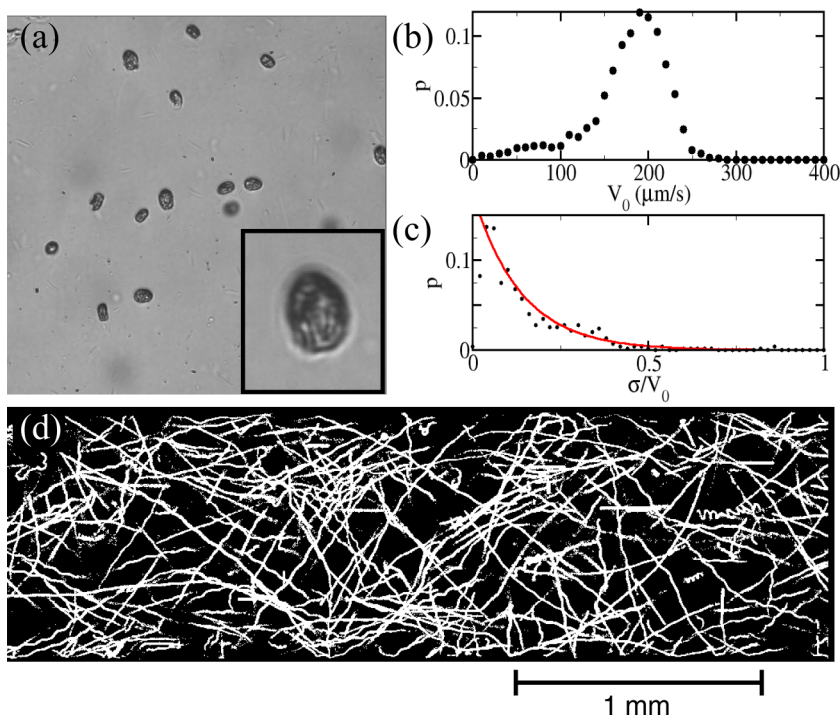


FIG. 6. (a) *Tetraselmis* microbes imaged at 40 $\times$  magnification. The inset is a zoom-in of one of the microbes. (b) Probability distribution of averaged swimming speeds  $V_0$  (averaged over the duration of each trajectory) for the microbes. (c) Variation of swimming speeds for individual microbes, plotted as the ratio of the standard deviation of the swimming speed divided by the average swimming speed for that microbe. The red curve shows a fit to a function  $p = ae^{-b\sigma/V_0}$  with  $a = 0.17$  and  $b = 7.3$ . (d) Ten-second streak image of the swimming *Tetraselmis* microbes at 4 $\times$  in the experimental apparatus with no flow. Movies of this image can be found online as Movie2.mpg and Movie3.mpg [46].

the average swimming speed for that microbe, with an average  $\langle \sigma/V_0 \rangle = 0.14$  for the microbes in these experiments.

In the absence of a flow [Fig. 6(d)], some microbes swim smoothly for extended periods of time. But some microbes in the same experiments tumble frequently. Subtle wiggling can also be seen in some of the trajectories when microbes swim in spiral patterns, due to slight symmetry-breaking in the flagella.

For experiments using 2 $\times$  magnification, we dye the *Tetraselmis* with fluorescein diacetate (FDA) [49,50] to improve the contrast in the imaging. Outside of a living cell, the FDA does not fluoresce. However, when FDA diffuses through the lipid bilayer into a microbe, enzymes inside the living cells cleave FDA to create fluorescein molecules. As such, this technique leads to fluorescent tagging only of living organisms. FDA does not seem to have any significant effects on the swimming of microbes. For dyed *Tetraselmis*, we use epi-fluorescence microscopy to increase the visibility of the algae and to enable tracking, even at low (2 $\times$ ) magnification.

We conducted tests of the microbes swimming in a cell without the magnets but with an imposed electrical current, and the electrical current was found not to have a significant effect on the swimming. Furthermore, the magnetic field produced by the permanent magnets below the cell appear to have negligible impact on the swimming behavior; in fact, the data about the behavior of *Tetraselmis* in the absence of a flow (Fig. 6) were collected with the *Tetraselmis* swimming in the cell with the permanent magnets.

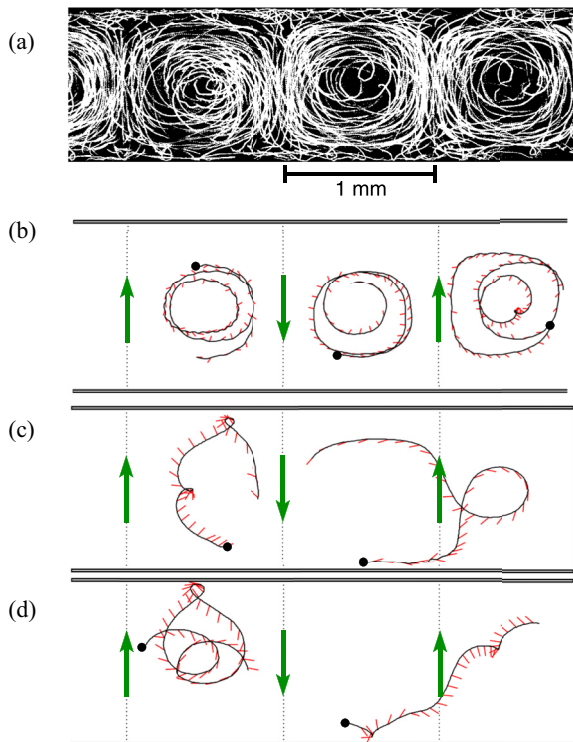


FIG. 7. (a) Ten-second streak image of microbes swimming in an imposed vortex flow, forced with a 2.0 mA electrical current;  $4\times$  magnification. Movies of this image can be found online in Supplemental Material as Movie4.mpg and Movie5.mpg [46]. (b–d) Sample trajectories (black curves) of microbes in the flow. The black dots show the start of the trajectory; the red segments show the swimming orientation, pointing away from the black curve; the dotted black lines show vortex separatrixes and the green arrows show the flow direction.  $v_0 = 0.2$  for (b) and  $v_0 = 0.4$  for panels (c) and (d).

In a typical experiment, there are up to a maximum of 50 microbes in the field of view at a time for  $4\times$  magnification and around 100 microbes at  $2\times$  magnification, with the densities dropping over the course of an experimental run. Densities of the microbes in the experiments range up to around 20 microbes per  $\text{mm}^2$  with typical separations around  $200\ \mu\text{m}$  or about 15–20 body lengths. So the interactions between the different algae are negligible in these studies.

### C. Procedures

The experiments done at  $4\times$  magnification [which are the basis for Figs. 6, 7, 8, and 16(a)] are from two different days of experiments with four different runs, while the experiments done at  $2\times$  magnification (which are the basis for the remaining experimental figures) are from seven different days with 20 separate runs. For each series of experiments, a couple of milliliters of fluid is drawn from one of the 15 ml centrifuge tubes containing cultured *Tetraselmis* using a pipette and slowly dribbled into the apparatus through a circular reservoir. (If the *Tetraselmis* are injected too quickly, they often do not swim well, presumably due to shearing of their flagella.) After settling for a minute or two, a 30–60 s run is recorded to verify if the *Tetraselmis* are swimming and to verify that there are no cross-flows through the apparatus. The focus of the microscope is also adjusted to be at the midheight of the cell, away from the top and bottom boundaries. If there is no cross-flow and if the microbes are swimming well, the electrical current is started to generate the vortex chain flow



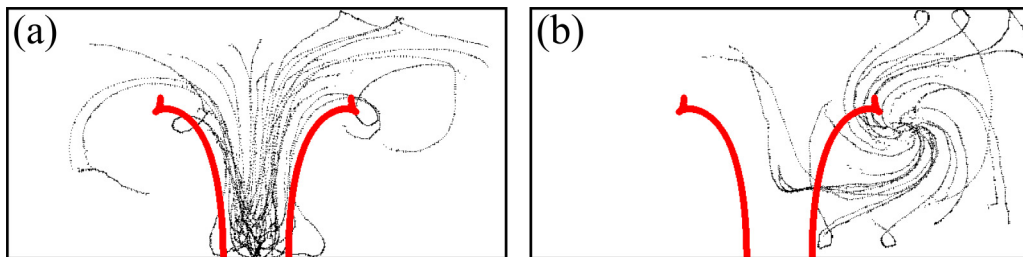


FIG. 8. Trajectories for  $v_0 = 0.4$  that start (a) near the bottom advective fixed point and (b) near the center of the right vortex. The red curves show two of the SWIM edges predicted from Eqs. (1) and (2), both of which block trajectories moving away from the separatrix and into the vortex centers. In both figures,  $x$  goes from 0 to 2 (i.e., two vortices) and  $y$  goes from 0 to 1 (one vortex) such that two full vortices are shown.

and another run is recorded. The duration of this run ranges from 5 minutes to 30 min, depending on microbes in the flow, with the run ending when the density has dropped to just a few microbes. (Typically, the microbes stop swimming after 20 - 30 minutes in the cell and settle to the bottom, out of the region of interest.) Additional runs during the same day are achieved by removing the fluid and injecting a fresh sample of *Tetraselmis* and repeating the process.

#### D. Tracking

We acquire images of the algae in the flow with an Andor Zyla sCMOS camera connected to the microscope. A background image is determined by averaging images for a half a minute. We subtract this background image from each subsequent image. We then threshold the subtracted images (keeping intensities for pixels above the threshold) and track the thresholded images in IDL with a package developed by Crocker and Weeks [51] that determines centroid coordinates for clusters of pixels (with each cluster identified as a microbe), and then links coordinates in successive frames to determine trajectories.

We fit the  $x(t)$  and  $y(t)$  coordinates of each trajectory to sliding parabolas to determine the  $x$  and  $y$  components of the total velocity of the microbe as it moves through the flow. To determine the swimming velocity  $\mathbf{V}_s$  of a specific microbe in an imposed flow, we begin by subtracting the experimentally measured flow velocity  $\mathbf{u}_{\text{flow}}$  from the velocity of the overall trajectory:  $\mathbf{V}_s = \mathbf{V}_{\text{traj}} - \mathbf{u}_{\text{flow}}$ . From the swimming velocity, we determine the instantaneous swimming speed  $V_s$  and the swimming direction  $\theta = \arctan(V_{sy}/V_{sx})$ . To compare with the theoretical predictions, we approximate  $V_0$  by the average of the swimming speed over a trajectory:  $V_0 = \langle V_s \rangle$ . And the dimensionless swimming speed is given by  $v_0 \equiv V_0/U$  where  $U$  is the maximum flow speed.

The theory of Eqs. (2) assumes smooth swimming particles that do not change their swimming directions other than by hydrodynamic interactions. Earlier studies of swimming microbes in a hyperbolic flow used smooth-swimming bacteria [26], but the *Tetraselmis* in these studies do not always swim smoothly. We analyze the trajectories to determine cases where the microbes suddenly change their swimming directions. We do this by identifying instances in trajectories where the angular velocity of the microbes differs greatly from the angular velocity predicted by the  $\dot{\theta}$  expression in Eqs. (2). This gives us the ability approximately to identify microbe trajectories that are mostly smooth versus those characterized by sudden tumble events.

When displaying the trajectories, we can use the symmetry of the flow to combine trajectories from different locations and different times. We shift trajectories horizontally by even multiples of the vortex width. We can combine these trajectories on the same plots as those shifted horizontally by odd multiples of the vortex width, but flipped vertically. For instance, a trajectory that crosses between vortices 3 and 4 can be shifted to the left by two vortices and displayed as though crossing between vortices 1 and 2. A trajectory that crosses between vortices 2 and 3 can be shifted to

the left by one vortex and flipped upside down. Furthermore, we sort the trajectories based on the nondimensional swimming speeds  $v_o = V_0/U$  determined from the velocity subtraction. The result is different groups of trajectories, with each group consisting of trajectories within a range of  $v_0$ . The net result is that we can display multiple trajectories in the same figure, even though these microbes are often in different vortices and are swimming in the region of interest at different times.

## IV. RESULTS

### A. Trajectories

Figure 7(a) shows a representative streak image for *Tetraselmis* trajectories in an imposed vortex flow. The swimming of the microbes is evident in this figure, with the microbe trajectories frequently crossing each other, something that is not possible for passive tracers in a 2D, time-independent flow.

Figures 7(b)–7(d) shows microbe trajectories (black curves) with their swimming directions shown as red segments, pointing away from the black curves. Loops and cusps are common in the microbe trajectories. Since  $\alpha$  is close to zero for the *Tetraselmis*, rotation of the swimmer is correlated strongly to the vorticity [see Eq. (2)], with the microbes forming loops in the regions with strongest vorticity [compare trajectories in Figs. 7(b)–7(d) to the vorticity field in Fig. 5(b)].

The right trajectory in the Fig. 7(c) (which is similar to the simulated trajectory in Fig. 4) shows a microbe moving back and forth between adjacent vortices. The microbe is initially in the middle vortex but is swimming to the right as it approaches and crosses over into the right-most vortex. After going through a loop, the microbe is swimming toward the left and crosses back into the previous vortex. This alternating between vortices is similar to the predicted [42,45] chaotic behavior of self-propelled tracers in vortex flows, although we cannot definitively conclude that this is deterministic chaotic motion from our data since there is the possibility of active tumbling in the microbe’s swimming. For slower swimming speeds [Fig. 7(b)], some trajectories are confined within a vortex, consistent with predictions of trapping of active particles in vortex flows [44,45].

### B. SwIMs and SwIM edges

The SwIMs and SwIM edges play a prominent role in the trajectories of microbes moving within and between vortices. Plots of trajectories demonstrate the one-way nature of the SwIM edges as barriers, as shown in Fig. 8. Figure 8(a) shows microbe trajectories that start in a small box around the flow’s fixed point at the bottom of the separatrix between adjacent vortices. Since the SwIM edges (in red) block in the direction pointing away from the separatrix, the microbes mostly do not penetrate and instead have to go around the SwIM edges. Penetration of the SwIM edges at the bottom is due to the fact that whereas the SwIM edges are calculated with a simplified model of the velocity field, Eqs. (1), with free-slip boundary conditions, the experimental velocity field has no-slip boundary conditions, with the fluid velocity going to zero at the bottom. There is no barrier to microbe movement if the fluid speed is less than the swimming speed of the microbe, as is the case near  $y = 0$  and 1. Microbe trajectories starting near and moving away from the vortex center [Fig. 8(b)] pass easily through the SwIM edges, which do not block trajectories moving outward from the vortex centers.

If we look just at trajectories that cross from one vortex to the next, we can see that the structure of these trajectories in  $(x, y, \theta)$  space (Fig. 9) is qualitatively similar to the chute structure formed by the SwIMs [Fig. 3(a)]. Densities of these trajectories projected into  $(x, y)$  space and cross-sections in  $(x, \theta)$  space are shown in Fig. 10 (for the mostly smooth-swimming trajectories) and in Fig. 11 (for trajectories with identified active tumbling events). We also plot stable and unstable SwIM edges predicted from the model (for the  $(x, y)$  projections) and cross-sections of the SwIMs [for the  $(x, \theta)$  cross-sections] in these figures. The predicted SwIM edges and cross-sections are determined from Eqs. (1) and (2) for the same  $v_0$  with  $\alpha = 0.3$ .

The approximate blocking behavior of the SwIM edges is evident in these figures. (There is slight breaching of these barriers due to the nonconstant swimming speed and the no-slip boundary

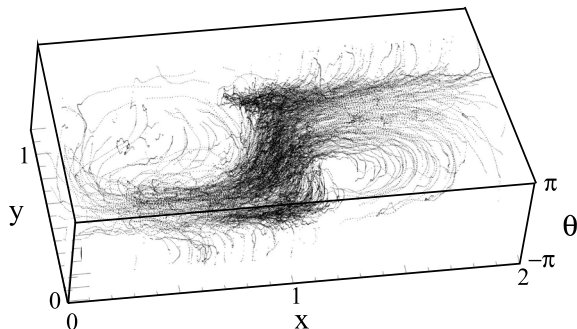


FIG. 9. Trajectories in  $(x, y, \theta)$  space of microbes with  $v_0 = 0.4$  that cross vortex boundaries.

conditions at  $y = 0$  and  $1$ .) For the trajectories with no active tumbling (Fig. 10), there is a slight  $x$ -asymmetry visible, with a lower density near the unstable SwIM edge and SwIM cross-sections (red) of the lower swimming fixed point versus near the stable SwIM edge (green) and cross-sections of the upper swimming fixed point. We do not have a complete explanation for this slight asymmetry; perhaps it is due to selection bias since only the trajectories that cross between vortices are included in Fig. 10. The asymmetry is less pronounced for the trajectories that include the active tumbling events (Fig. 11).

### C. Densities and swimming orientations

Based on Eqs. (1) and (2), mixing of perfectly spherical ( $\alpha = 0$ ) swimmers in an incompressible flow is divergence free in  $(x, y, \theta)$  space. *Tetraselmis*, however, are not perfectly spherical, and there is also a question of how the flagella affect the value of  $\alpha$ . Consequently, density variations are

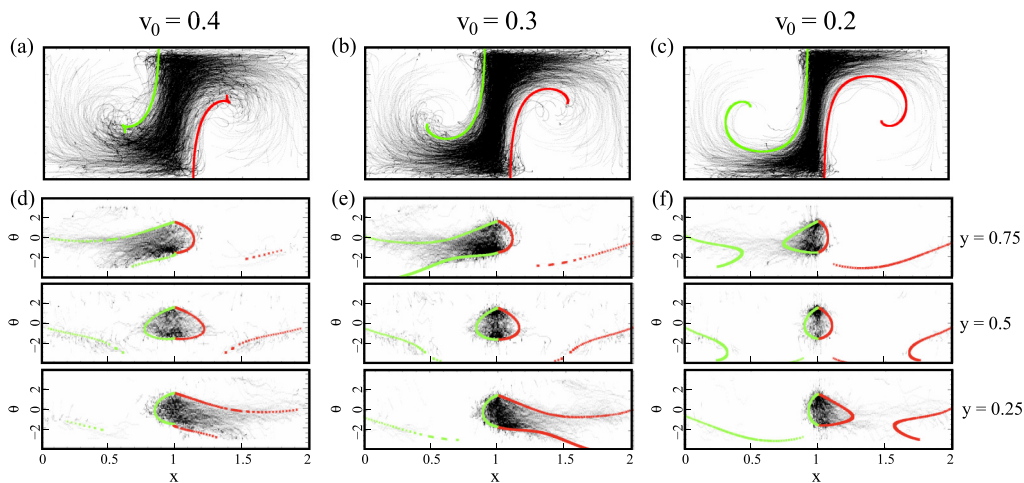


FIG. 10. Smooth-swimming trajectories that cross between vortices. (a–c) Density in  $(x, y)$  of crossing trajectories. In each of these figures, the red (green) curves show the unstable (stable) SwIM edge of the bottom (top) swimming fixed point, calculated from Eqs. (1) and (2) with  $\alpha = 0.3$ . (d–f) Cross-sections in  $(x, \theta)$  of crossing trajectories. In each figure, the top, middle, and bottom panels correspond to slices at  $y = 0.75$ ,  $0.50$ , and  $0.25$  in dimensionless units. Cross sections of the predicted right-going chute—which is the stable and unstable SwIMs— are shown in each panels (d–f).

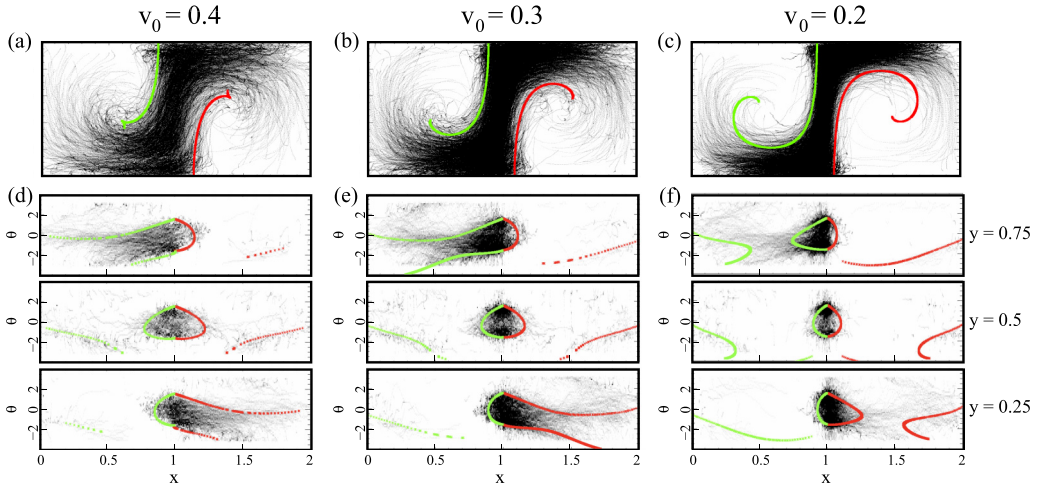


FIG. 11. All trajectories—including those that tumble—that cross between vortices. (a–c) Density in  $(x, y)$  of crossing trajectories. In each of these figures, the red (green) curves show the unstable (stable) SwIM edge of the bottom (top) swimming fixed point, calculated from Eqs. (1) and (2) with  $\alpha = 0.3$ . (d–f) Cross-sections in  $(x, \theta)$  of crossing trajectories. In each figure, the top, middle and bottom panels correspond to slices at  $y = 0.75, 0.50$  and  $0.25$  in dimensionless units. Cross sections of the predicted right-going chute—which is the stable and unstable SwIMs— are shown in each of panels (d–f).

possible in  $(x, y, \theta)$  space. We take trajectories for a given range of  $v_0$  and determine histograms of the locations of these trajectories in  $(x, y, \theta)$ . Figure 12 shows  $(x, y)$  slices of these histograms for  $v_0 = 0.2$  and  $0.4$ . For the smaller nondimensional swimming speed [Figs. 12(a)–12(d)], some clear variations in density are apparent, with a higher density in the vicinity of the vortex separatrices for rightward- and leftward-swimming microbes [Figs. 12(b) and 12(d), respectively].

Density variations are also visible in  $(x, \theta)$  and  $(y, \theta)$  slices of the histograms (Figs. 13 and 14, respectively). Slower swimming ( $v_0 = 0.2$ ) microbes swimming in the vicinity of the vortex separatrices [Figs. 14(a) and 14(c) and the edges and middle of Fig. 13(c)] have a clear preference to be swimming with orientation parallel or anti-parallel to the flow along the separatrices. Microbes swimming near the bottom and top boundaries [ $y = 0$  and  $1$ , Figs. 13(a) and 13(e)] have a preference to be oriented swimming parallel to those boundaries. This is consistent with a recent theoretical study [52] that indicates that microbes swimming near a solid boundary have a higher probability to swim parallel to that boundary in the absence of a flow.

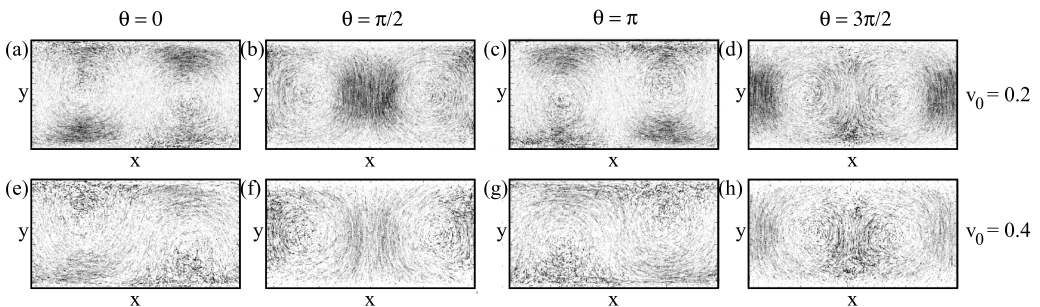


FIG. 12.  $(x, y)$  slices of histogram with  $x$  from 0 to 2 (starting and finishing at vortex edges) and  $y$  from 0 to 1;  $v_0$  and  $\theta$  values are displayed on the image.



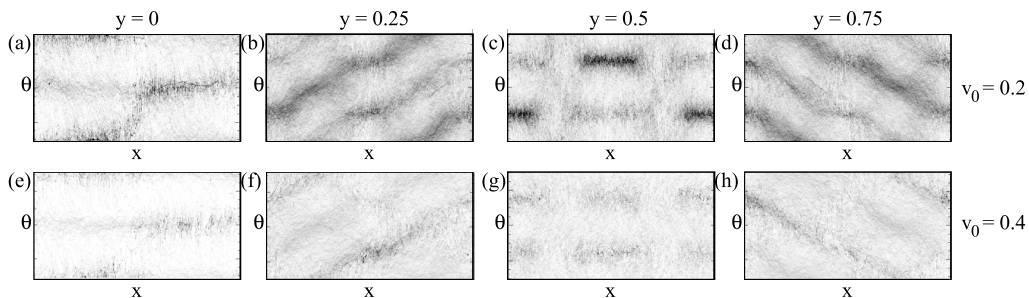


FIG. 13.  $(x, \theta)$  slices of histogram with  $x$  from 0 to 2 and  $\theta$  from  $-\pi$  to  $\pi$ ;  $v_0$  and  $y$  values are shown in the figure.

The preferred swimming orientation can be seen by plotting probability functions  $p(\theta)$  for the swimmer orientations, as shown in Fig. 15 for swimmers near the center of the separatrices between adjacent vortices, i.e., near  $(x, y) = (0, 0.5)$  or  $(1, 0.5)$  in nondimensional units. The microbes tend to align with the flow, more so for smaller nondimensional swimming speed  $v_0 = 0.2$  [Figs. 15(a) and 15(b)] than for the larger speed  $v_0 = 0.4$  [Figs. 15(c) and 15(d)]. This is consistent with the previous study of active mixing of microbes in a hyperbolic flow [27] which found more pronounced orientations for larger flow speed (which also reduces the nondimensional swimming speed).

#### D. Flux and chutes

In addition to blocking motion of the microbes within the vortices, the manifolds determine transport of microbes from one vortex to the next. Figures 10(d)–10(f) and 11(d)–11(f) show  $(x, \theta)$  cross sections of the crossing trajectories along with cross sections of the right-going chute (see Fig. 3) formed from theoretical SwIMs calculated from Eqs. (1) and (2). (These SwIMs are approximate, calculated with free-slip boundary conditions and with  $\alpha = 0.3$ .) The points well outside the SwIM cross sections correspond to microbes that have circled back around the vortex after crossing the separatrix. Overall, there is good agreement—especially at  $y = 0.5$  away from the

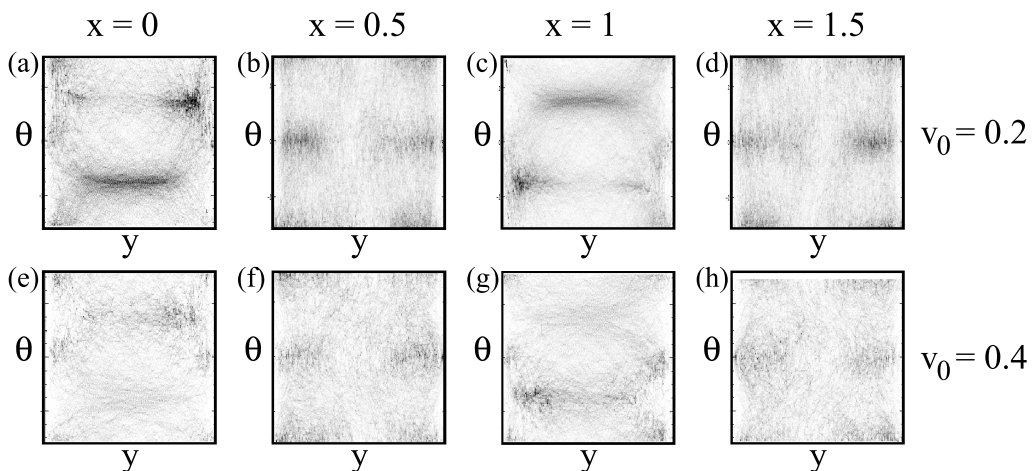


FIG. 14.  $(y, \theta)$  slices of histogram with  $y$  from 0 to 1 and  $\theta$  from  $-\pi$  to  $\pi$ ;  $v_0$  and  $x$  values are shown in the figure.

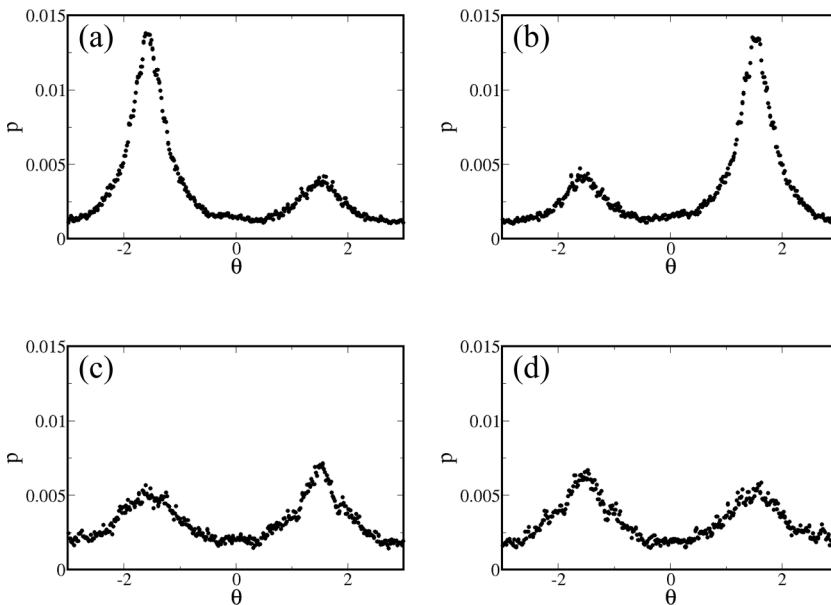


FIG. 15. PDF of swimming angles at middle and left/right separatrices. (a)  $v_0 = 0.2$ ,  $x = 0$ ,  $y = 0.5$ ; (b)  $v_0 = 0.2$ ,  $x = 1$ ,  $y = 0.5$ ; (c)  $v_0 = 0.4$ ,  $x = 0$ ,  $y = 0.5$ ; (d)  $v_0 = 0.4$ ,  $x = 1$ ,  $y = 0.5$ .

no-slip boundary conditions that are not captured in the simulations—indicating that the chutes do, in fact, act as the portals that carry active tracers between adjacent vortices.

The flux of microbes crossing the vortex separatrices in the experiments can be compared to that predicted by the chute mechanism. The starting locations of microbes that cross a separatrix in a time  $t$  are shown in Fig. 16(a) for two different times, along with envelopes for four different delay times. The growing area of the region of active particles crossing the separatrix—and, consequently, the flux between vortices—is represented in Fig. 16(b) by plotting the fraction of microbes that escape the vortex in a defined time interval. Figure 16(b) also shows the predictions, Eq. (3), for this growing fraction, based on the chute analysis. The inset shows the flux

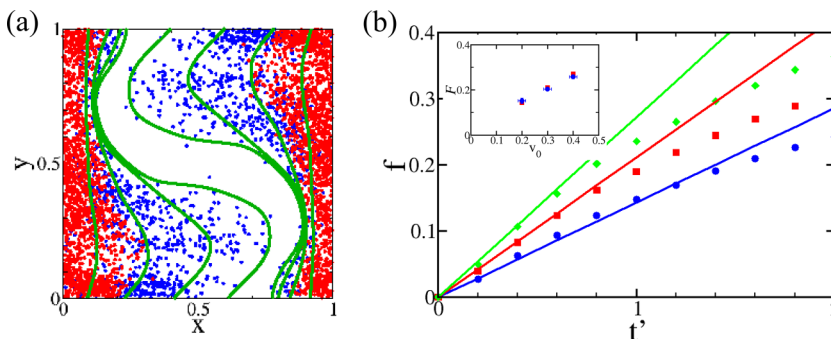


FIG. 16. (a) Initial locations of microbes with  $v_0 = 0.4$  that cross either vortex separatrix in time  $t = 0.8$  s (red dots) and  $t = 1.6$  s (blue dots); the green curves show the envelopes for times  $t = 0.4, 0.8, 1.2$ , and  $1.6$  s (nondimensional times 0.27, 0.53, 0.80, and 1.1). (b) Fraction of microbes with no active tumbling that escape the vortex in a nondimensional time  $t' = tU/L$  in experiments (symbols) and theory (lines);  $v_0 = 0.2$  (blue), 0.3 (red), and 0.4 (green). The inset shows the flux  $F = df/dt'$  for small times ( $t' < 0.8$ ) for the experimental data (blue circles) and predictions (red squares) from Eq. (3).



$F = df/dt'$  for the predictions and for the small time limit in the experimental results. (The error bars for  $F$  in the inset—which are comparable to the size of the symbols—expresses the range of slopes calculated with different ranges of data between  $t' = 0$  and  $t' = 0.8$ . The uncertainty in  $v_0 \equiv V_0/U$  is dominated by uncertainty in the measured value of  $U$ .) The measured flux  $F$  for small times is consistent (within uncertainties) with the prediction based on the cross-sectional chute area.

## V. DISCUSSION

The nature of swimming invariant manifolds (SwIMs) as barriers for the mixing of swimming microbes in a vortex flow is clear from these experiments, as is the importance of chutes (composed of combinations of SwIMs) as a fundamental mechanism for cross-vortex transport. The consistency between the experimental flux of microbes between vortices and the predictions from the chute mechanism is notable despite the fact that the prediction, Eq. (3), assumes uniform microbe densities in  $(x, y, \theta)$  space, which is clearly not the case—especially for smaller  $v_0$ —as seen in Figs. 12–14. There are additional differences between the model used for the prediction and the experimental data: (a) the experiments have no-slip boundary conditions, whereas the predictions use a simpler free-slip model; (b) there is Ekman pumping [34] in the experiments that causes a slight, 3D recirculation within the vortices; (c) the microbes are not ideal smooth swimmers—even accounting for our technique that excludes active tumbling from the analysis, there is also noise and oscillations in their orientation that allow trajectories to cross the SwIMs; and (d) the theory does not take into account interactions of the swimming microbes with the fixed walls [52]. It is quite striking that the SwIM theory works as well as it does for this nonideal experimental system, indicating robustness of the approach.

Experiments are on-going to characterize long-range transport of active particles in an extended chain or array of vortices. The chute mechanism discussed in this paper merely describes the method for swimmers to cross from one vortex to the next. The long-range transport properties are determined by several factors including not just the short-term flux but also the coexistence of ordered and chaotic regions which can give rise to long-range transport that is nondiffusive [53].

Another very interesting question is the effect of flagella on the value of  $\alpha$  for the swimming organism and its effect on swimming orientations through the  $\dot{\theta}$  equation in Eqs. (2). In fact, the effect of the flagella on  $\alpha$  might even depend on the nondimensional swimming speed  $v_0$ . It may be possible to measure  $\alpha$  experimentally from orientation distributions similar to those in Fig. 15, although that analysis is likely more straightforward for the experiments done with microbes in hyperbolic flows [26,27]. This is an ongoing area of study.

Additional studies in the future might include experiments with more elongated swimmers to test the validity of the SwIM theory for swimmers with  $\alpha$  closer to 1. As we saw for experiments with hyperbolic flows [27] (and as is expected by the theory), density variations in  $(x, y, \theta)$  space are more significant for swimmers with  $\alpha$  closer to 1, which might also affect the flux between vortices. Another important question is the effects on the SwIMs of noise and active tumbling in the swimming as well as chemotaxis, issues that are relevant to determining how robust SwIM approaches are for understanding the mixing of realistic swimmers in nature. The combined mixing of both passive and active particles in a flow is of interest, particularly if the passive impurity is the nutrients to which the active particles are chemotactic. We are also interested in the effects of SwIMs on collective behavior [54] in experiments with larger microbe densities.

Ultimately, we are interested in possible extensions of the manifold and chute approach to time-periodic and time-aperiodic flows. For time-periodic flows, remnants of invariant tori [47] could play a significant role on transport and mixing of active particles. For aperiodic and turbulent flows, extensions of the SwIM approach might be possible, in analogy with *Lagrangian coherent structure* approaches [55,56] which extended passive manifold theories characterizing passive mixing in time-aperiodic and turbulent flows.

### ACKNOWLEDGMENTS

These experiments were supported by the National Science Foundation under Grants No. DMR-1806355, No. DMR-2302708, and No. CMMI-2314417. The authors thank Jack Raup, Joe Tolman, and Brian Garthwaite for assistance with the microfluidic cells.

---

- [1] M. C. Marchetti, J. F. Joanny, S. Ramaswamy, T. B. Liverpool, J. Prost, M. Rao, and R. A. Simha, Hydrodynamics of soft active matter, *Rev. Mod. Phys.* **85**, 1143 (2013).
- [2] H. C. Berg and R. A. Anderson, Bacteria swim by rotating their flagellar filaments, *Nature (London)* **245**, 380 (1973).
- [3] W. Wang, X. Lv, J. L. Moran, S. Duan, and C. Zhou, A practical guide to active colloids: Choosing synthetic model systems for soft matter physics research, *Soft Matter* **16**, 3846 (2020).
- [4] S. J. Ebbens and J. R. Howse, In pursuit of propulsion at the nanoscale, *Soft Matter* **6**, 726 (2010).
- [5] S. Das, A. Garg, A. I. Campbell, J. Howse, A. Sen, and D. Velegol, Boundaries can steer active Janus spheres, *Nat. Commun.* **6**, 8999 (2015).
- [6] A. Kaiser, A. Snezhko, and I. S. Aranson, Flocking ferromagnetic colloids, *Sci. Adv.* **3**, e1601469 (2017).
- [7] X. Xu, S. Hou, N. Wattanatorn, F. Wang, Q. Yang, C. Zhao, X. Yu, H.-R. Tseng, S. J. Jonas, and P. S. Weiss, Precision-guided nanospikes for targeted and high-throughput intracellular gene delivery, *ACS Nano* **12**, 4503 (2018).
- [8] S. Bialonski, D. A. Caron, J. Schloen, U. Feudel, H. Kantz, and S. D. Moorthi, Phytoplankton dynamics in the southern california bight indicate a complex mixture of transport and biology, *J. Plankton Res.* **38**, 1077 (2016).
- [9] S. Futatani, D. del-Castillo-Negrete, X. Garbet, S. Benkadda, and N. Dubuit, Self-consistent dynamics of impurities in magnetically confined plasmas:turbulence intermittency and nondiffusive transport, *Phys. Rev. Lett.* **109**, 185005 (2012).
- [10] R. Rusconi, J. S. Guasto, and R. Stocker, Bacterial transport suppressed by fluid shear, *Nat. Phys.* **10**, 212 (2014).
- [11] A. Dehkharghani, N. Waisbord, J. Dunkel, and J. S. Guasto, Bacterial scattering in microfluidic crystal flows reveals giant active Taylor-Aris dispersion, *Proc. Natl. Acad. Sci. USA* **116**, 11119 (2019).
- [12] S. A. Berman and K. A. Mitchell, Swimming dynamics in externally driven flows: The role of noise, *Phys. Rev. Fluids* **7**, 014501 (2022).
- [13] S. A. Berman, K. S. Ferguson, N. Bizzak, T. H. Solomon, and K. A. Mitchell, Noise-induced aggregation of swimmers in the Kolmogorov flow, *Front. Phys.* **9**, 816663 (2022).
- [14] X.-L. Wu and A. Libchaber, Particle diffusion in a quasi-two-dimensional bacterial bath, *Phys. Rev. Lett.* **84**, 3017 (2000).
- [15] K. C. Leptos, J. S. Guasto, J. P. Gollub, A. I. Pesci, and R. E. Goldstein, Dynamics of enhanced tracer diffusion in suspensions of swimming eukaryotic microorganisms, *Phys. Rev. Lett.* **103**, 198103 (2009).
- [16] T. V. Kasyap, D. L. Koch, and M. Wu, Hydrodynamic tracer diffusion in suspensions of swimming bacteria, *Phys. Fluids* **26**, 081901 (2014).
- [17] R. Ran, Q. Brosseau, B. C. Blackwell, B. Qin, R. L. Winter, and P. E. Arratia, Bacteria hinder large-scale transport and enhance small-scale mixing in time-periodic flows, *Proc. Natl. Acad. Sci. USA* **118**, e2108548118 (2021).
- [18] L. Abbaspour and S. Klumpp, Enhanced diffusion of a tracer particle in a lattice model of a crowded active system, *Phys. Rev. E* **103**, 052601 (2021).
- [19] J. Mahoney, D. Bargteil, M. Kingsbury, K. Mitchell, and T. Solomon, Invariant barriers to reaction front propagation in fluids flows, *Europhys. Lett.* **98**, 44005 (2012).
- [20] D. Bargteil and T. Solomon, Barriers to front propagation in ordered and disordered vortex flows, *Chaos* **22**, 037103 (2012).

- [21] K. A. Mitchell and J. R. Mahoney, Invariant manifolds and the geometry of front propagation in fluid flows, *Chaos* **22**, 037104 (2012).
- [22] P. W. Megson, M. L. Najarian, K. E. Lilienthal, and T. H. Solomon, Pinning of reaction fronts by burning invariant manifolds in extended flows, *Phys. Fluids* **27**, 023601 (2015).
- [23] S. Gowen and T. Solomon, Experimental studies of coherent structures in an advection-reaction-diffusion system, *Chaos* **25**, 087403 (2015).
- [24] J. R. Mahoney, J. Li, C. Boyer, T. Solomon, and K. A. Mitchell, Frozen reaction fronts in steady flows: A burning-invariant-manifold perspective, *Phys. Rev. E* **92**, 063005 (2015).
- [25] M. Doan, J. J. Simons, K. Lilienthal, T. Solomon, and K. A. Mitchell, Barriers to front propagation in laminar, three-dimensional fluid flows, *Phys. Rev. E* **97**, 033111 (2018).
- [26] S. A. Berman, J. Buggeln, D. A. Brantley, K. A. Mitchell, and T. H. Solomon, Transport barriers to self-propelled particles in fluid flows, *Phys. Rev. Fluids* **6**, L012501 (2021).
- [27] H. Yoest, J. Buggeln, M. Doan, P. Johnson, S. A. Berman, K. A. Mitchell, and T. H. Solomon, Barriers impeding active mixing of swimming microbes in a hyperbolic flow, *Front. Phys.* **10**, 861616 (2022).
- [28] R. S. MacKay, J. D. Meiss, and I. C. Percival, Transport in Hamiltonian systems, *Physica D* **13**, 55 (1984).
- [29] T. H. Solomon and J. P. Gollub, Chaotic particle transport in time-dependent Rayleigh-Bénard convection, *Phys. Rev. A* **38**, 6280 (1988).
- [30] T. H. Solomon and J. P. Gollub, Passive transport in steady Rayleigh-Bénard convection, *Phys. Fluids* **31**, 1372 (1988).
- [31] S. Wiggins, *Chaotic Transport in Dynamical Systems* (Springer-Verlag, New York, NY, 1992).
- [32] R. Camassa and S. Wiggins, Chaotic advection in a Rayleigh-Bénard flow, *Phys. Rev. A* **43**, 774 (1991).
- [33] T. H. Solomon, S. Tomas, and J. L. Warner, Role of lobes in chaotic mixing of miscible and immiscible impurities, *Phys. Rev. Lett.* **77**, 2682 (1996).
- [34] T. H. Solomon and I. Mezić, Uniform resonant chaotic mixing in fluid flows, *Nature (London)* **425**, 376 (2003).
- [35] G. A. Voth, G. Haller, and J. P. Gollub, Experimental measurements of stretching fields in fluid mixing, *Phys. Rev. Lett.* **88**, 254501 (2002).
- [36] M. Mathur, G. Haller, T. Peacock, J. E. Ruppert-Felsot, and H. L. Swinney, Uncovering the Lagrangian skeleton of turbulence, *Phys. Rev. Lett.* **98**, 144502 (2007).
- [37] C. Coulliette, F. Lekien, J. D. Paduan, G. Haller, and J. E. Marsden, Optimal pollution mitigation in Monterey bay based on coastal radar data and nonlinear dynamics, *Environ. Sci. Technol.* **41**, 6562 (2007).
- [38] H. Aref, Stirring by chaotic advection, *J. Fluid Mech.* **143**, 1 (1984).
- [39] J. M. Ottino, *The Kinematics of Mixing: Stretching, Chaos and Transport* (Cambridge University Press, Cambridge, UK, 1989).
- [40] V. Rom-Kedar, Homoclinic tangles—Classification and applications, *Nonlinearity* **7**, 441 (1994).
- [41] C. Torney and Z. Neufeld, Transport and aggregation of self-propelled particles in fluid flows, *Phys. Rev. Lett.* **99**, 078101 (2007).
- [42] N. Khurana, J. Blawdziewicz, and N. T. Ouellette, Reduced transport of self-propelled particles in fluid flows, *Phys. Rev. Lett.* **106**, 198104 (2011).
- [43] A. Zöttl and H. Stark, Nonlinear dynamics of a microswimmer in Poiseuille flow, *Phys. Rev. Lett.* **108**, 218104 (2012).
- [44] J.-A. Arguedas-Leiva and M. Wilczek, Microswimmers in an axisymmetric vortex flow, *New J. Phys.* **22**, 053051 (2020).
- [45] S. A. Berman and K. A. Mitchell, Trapping of swimmers in a vortex lattice, *Chaos* **30**, 063121 (2020).
- [46] See Supplemental Material at <http://link.aps.org/supplemental/10.1103/PhysRevFluids.9.054501> for movies corresponding to Figs. 4(a), 6(d), and 7(a).
- [47] E. Ott, *Chaos in Dynamical Systems*, 2nd ed. (Cambridge University Press, Cambridge, UK, 2002).
- [48] H. Willaime, O. Cardoso, and P. Tabeling, Spatiotemporal intermittency in lines of vortices, *Phys. Rev. E* **48**, 288 (1993).
- [49] J. M. Widholm, The use of fluorescein diacetate and phenosafranine for determining viability of cultured plant cells, *Stain Technol.* **47**, 189 (1972).

- [50] M. Onji, T. Sawabe, and Y. Ezura, An evaluation of viable staining dyes suitable for marine phytoplankton, *Bull. Fac. Fish. Hokkaido Univ.* **51**, 153 (2000).
- [51] J. C. Crocker and E. R. Weeks, Particle tracking using IDL, Available at <http://physics.emory.edu/faculty/weeks/idl/> (2011).
- [52] H. Chen and J.-L. Thiffeault, Shape matters: A Brownian microswimmer in a channel, *J. Fluid Mech.* **916**, A15 (2021).
- [53] M. F. Schlesinger, G. M. Zaslavsky, and J. Klafter, Strange kinetics, *Nature (London)* **363**, 31 (1993).
- [54] J. Dunkel, S. Heidenreich, K. Drescher, H. H. Wensink, M. Bär, and R. E. Goldstein, Fluid dynamics of bacterial turbulence, *Phys. Rev. Lett.* **110**, 228102 (2013).
- [55] A. Hadjighasem, M. Farazmand, D. Blazeovski, G. Froyland, and G. Haller, A critical comparison of Lagrangian methods for coherent structure detection, *Chaos* **27**, 053104 (2017).
- [56] S. Balasuriya, N. T. Ouellette, and I. I. Rypina, Generalized Lagrangian coherent structures, *Physica D* **372**, 31 (2018).